Supplementary Information

Controlling the oxidation and chemistry of photodeposited CuO_X species via charge density modulation

Szymon Dudziak[*], *Marta Kowalkińska, José D. Gouveia, Adam Ostrowski, Miguel Gomez-Mendoza, Marcin Łapiński, Aleksandra Szkudlarek, José R. B. Gomes, Víctor A. de la Peña O'Shea and Anna Zielińska-Jurek*

[*]*Correspondence*: szymon.dudziak@pg.edu.pl

Experimental

S1. Photocatalyst preparation:

Photocatalysts preparation was conducted hydrothermally, following previous studies.[1,2] Briefly, 40 cm^3 of TBT was mixed inside a 200 cm^3 Teflon-lines reactor with 40 cm^3 of ethanol and 8 cm^3 of HF solution (48 % wt.). After mixing for a few minutes, the reactor was closed and placed in the oven at 180 °C for 10 h (including heating). After the reactions, the reactor was placed out, cooled naturally and the product was collected. Obtained powders were centrifuged at 6000 rpm and washed 3 times with ethanol, followed by washing with water. During the water washing, the suspension was systematically neutralized with 0.1 M NaOH solution until: (1) the pH of the solution was stable at ≈7 and (2) particles were easily separated without further NaOH introduction. After this point, the samples were washed 5 times with water only, dried at 60 °C and hand-ground in agate mortar.

For analyzing the different doping effects, $NbCl_5$, $GaCl_3$, $Sc(NO_3)_3{\cdot}xH_2O$ or $AlCl_3{\cdot}6H_2O$ were dissolved in a part of the ethanol and introduced to the synthesis. In case of an Sc-modified sample, the overall synthesis was scaled-down to ¼ of the presented amounts. For the Ga and Nb-modified materials, both chlorides were used directly after receiving them from the manufacturer.

Modification with CuO_x was performed via photodeposition of the $CuSO_4$ salt from the water/methanol mixture (50/50 v/v). Briefly, 0.2 g of the photocatalyst was dispersed using an ultrasound bath with a corresponding amount of Cu^{2+} added from the concentrated solution. The vial was then placed in a black box and purged with nitrogen for 30 minutes under continued magnetic stirring. After this time, the suspension was irradiated with a Xe lamp for 1 h without removing N_2 or stirring. During the whole process, the vial was closed with a rubber plug, leaving a slight leakiness for the N_2 to escape. Modified photocatalysts were centrifuged and washed with water 3 times, followed by drying at 80 °C.

S2. Materials characterization:

The crystal structure of the obtained materials was investigated using the powder XRD method with a Rigaku MiniFlex 600 diffractometer (Cu Kα radiation). Phase identification and profile refinements were performed based on the available .cif files of the possible crystal phases.[3,4] Absorbance of the samples was studied with the Thermo Fisher Scientific Evolution 220 spectrophotometer in the 250-1100 nm range, with $BaSO_4$ acting as reflectance standard. Transmission electron microscope images were collected using TEM TECNAI TF 20 X-TWIN, equipped with the field emission gun and operating at 200 kV. Analysis of the selected area electron diffraction patterns and corresponding zone-axes were performed using CrystBox software[5,6] and the available .cif file of the anatase crystal structure. Chemical composition and the chemical states of the elements at the surface were determined with X-ray Photoelectron

Spectroscopy (XPS) measurements, carried out using a 128-channel Argus hemispherical analyser (Omicron NanoTechnology, Taunusstein, Germany) equipped with a magnesium Kα X-ray source, operated at 15 keV and 300 W. High-resolution spectra were collected at room temperature under ultra-high vacuum conditions (pressure below 1.1×10^{-8} mbar). Data processing and spectral deconvolution were performed using the CASA XPS software package, employing Shirley-type background subtraction and peak fitting with a Gauss-Lorentz (GL 30) function via the least squares optimization method. The binding energy scale was calibrated by setting the C 1*s* peak to 285.00 eV. Electron paramagnetic resonance (EPR) spectra of powdered samples were recorded down to 80 K using a BRUKER ELEXSYS spectrometer (X-band). Temperature of the samples was controlled and stabilized with ITC 503S Oxford Instruments Temperature Controller For the photochemical EPR experiments, the samples were irradiated at 80 K, directly in the EPR resonator, with LG UV LED (3 W, λ_{max} = 365 nm) acting as a light source. The light power was about 70 $mW \cdot cm^{-2}$. Electrochemical measurements were performed using Autolab PGSTAT204 potentiostat–galvanostat with FRA32 M Module, using three-electrode system based on the commercial Metrohm DropSense DRP-11L screen-printed electrodes in 0.5 M KCl solution. The sample was deposited as a thin layer on the glassy carbon substrate and blocked with a drop of Nafion solution (1% wt. in isopropanol), while Ag/AgCl and glassy carbon served as a reference and counter electrodes, respectively. The Mott-Schottky analysis was performed based on the electrochemical impedance spectroscopy data, gathered with a 10 mV AC signal amplitude and a frequency of 1000 Hz. The space charge capacitance was determined with the standard formula $C=-(2\pi \cdot f \cdot Z_{im})^{-1}$. Steady-state photoluminescence emission spectra were recorded using Shimadzu RF-600 spectrofluorometer with excitation wavelength of 310 nm, excitation and emission bandwidths of 10/20 nm, respectively and with the 400 nm cut-filter at the emission side. Photoluminescence lifetimes were measured using a Mini-τ based on time-correlated single photon counting (TCSPC) from Edinburgh Instruments. As excitation source was used an EPL-375 picosecond pulsed diode laser at 372 nm with a pulse width of 61.2 ps (repetition rate of 1 MHz) from Edinburgh Instruments. An emission band-pass filter between 425-475 nm was used to monitor only the fraction where TiO_2 emits. The instrument response function (IRF) signal was measured as reference in all cases. Experimental data were fitted to bi-exponential fit.

S3. Computational studies:

The density-functional theory (DFT) calculations were performed with the VASP code.[7] The PBE functional[8] within the generalized gradient approximation was chosen for all calculations. Although a hybrid functional would be more suitable for the calculation of electronic properties, such as semiconductor band gap values,[9] PBE is known to provide accurate qualitative results and correctly describe the shapes of energy bands,[10,11] at a more manageable computational cost.

The simulations were run on periodic TiO_2 {0 0 1} supercells, containing 3 × 3 unit cells of this surface, with a total of 135 atoms and the most stable surface termination, as determined in Ref. 12.[12] For the doped systems, one Ti atoms was replaced with either Nb or Ga, resulting in an approximate concentration of 2.27% at. (relative to Ti). To ensure enough separation between periodic replicas of the system, 28 Å of vacuum were added in the direction perpendicular to the basal plane of the surface.

The explicitly treated electrons were $3p^6\ 3d^3\ 4s^1$ for Ti, $2s^2\ 2p^4$ for O, $3p^6\ 3d^{10}\ 4s^1$ for Cu, $4p^6\ 4d^4\ 5s^1$ for Nb, and $3d^{10}\ 4s^2\ 4p^1$ for Ga, with their wave functions expanded as plane waves, while the remaining electrons were included in the frozen core, handled by the projector augmented-wave method.[13] Brillouin zone integrations were done using 4 × 4 × 1 grids of special k-points, as prescribed by the Monkhorst-Pack method.[14] The energy cutoff for the plane-wave basis set was 415 eV, and the energy and force convergence thresholds were 10^{-5}

eV and 0.01 eV/Å, respectively. The transition states were located using the dimer method and characterized upon the calculation of a single imaginary vibrational wavenumber associated to the reaction coordinate.[15]

S4. Photocatalytic experiments and analytical procedures:

The photocatalytic activity was tested using a 40 cm^3 quartz reactor, equipped with a cooling jacket and magnetic stirrer, together with airflow introduction. For a typical reaction, 20 mg of the photocatalyst were dispersed in the reaction medium using ultrasound bath (few seconds) and the reactor was placed inside the black box under stirring, cooling (20 °C) and bubbling with air (4 $dm^3 \cdot h^{-1}$). The prepared system was stabilised for 10 minutes, after which the light was introduced. For most of the experiments, a 300 W Xe lamp was used as the light source, with the UVA flux reaching the reactor centre being 22 $mW \cdot cm^{-2}$. The lamp was equipped with a water filter and a 310 nm filter to cut off IR and high-energy UV radiation from the experiments. Alternatively, 385 nm high power LED source was used for the detailed calculations of the degradation quantum efficiencies, as shown in detail in section S15. All collected samples were passed through a 0.2 μm filter to remove photocatalyst particles.

Generation of ·OH was monitored using coumarin as a probe. Experiments were performed with the ~470 μM solution and the relative amount of generated ·OH was determined from the luminescence of the produced 7-hydroxycoumarin.[16] Luminescence was studied using a Shimadzu RF-6000 spectrofluorometer and the 7-hydroxycoumarin concentration was estimated from the performed calibration.

The generation of $\cdot O_2^-$ was determined using 4-chloro-7-nitrobenzofurazan (NBD-Cl) as a chemical probe.[17] Experiments were performed with the 0.5 mM solution and the relative amount of generated $\cdot O_2^-$ was determined as a characteristic 470 nm absorbance. The concentration of $\cdot O_2^-$ was then estimated using the known extinction coefficient of the product: 4000 $M^{-1} \cdot cm^{-1}$.[17]

The generation of H_2O_2 was determined using the iodometric method. The reaction was performed in a 10/90 mixture of isopropanol and water (v/v), with aeration increased to 10 $dm^3 \cdot h^{-1}$. For the procedure, 1 cm^3 of the collected sample was mixed with 1 cm^3 of the potassium phthalate solution (0.2 M) and 1 cm^3 potassium iodine solution (0.4 M) and left to react for 5 minutes in the dark. After this, the absorbance of the solution was measured and the H_2O_2 concentration was determined from the characteristic 350 nm absorbance, based on the performed calibration.

The photocatalytic degradation of phenol, EE2 (17α-ethinylestradiol), naphthalene, and methomyl ((*E*,*Z*)-methyl *N*-{[(methylamino)carbonyl]oxy}ethanimidothioate) was monitored using the Shimadzu HPLC system, combined with a diode-array detector. The concentration was estimated from the performed calibration (multi-point for phenol and single-point for other compounds).

Results and discussion

S5. Additional XRD and TEM results before CuO_x deposition:

Figure S1 show results of the initial trials of the acceptor doping of the {0 0 1} anatase nanoparticles. In case of the Sc^{3+} and Al^{3+}, some amounts of MF_3 phases were observed (**Figure S1a**).[18,19] No separate phase has formed when Ga^{3+} was introduced, which was further confirmed with the detailed, low-speed scan of bare and Ga-modified TiO_2 samples (**Figure S1b**). Simultaneously, **Figure S2** show further TEM images and additional shape analysis of the selected samples. Refinement data of further samples doped with Nb^{5+} and Ga^{3+} is presented in **Table S1**.

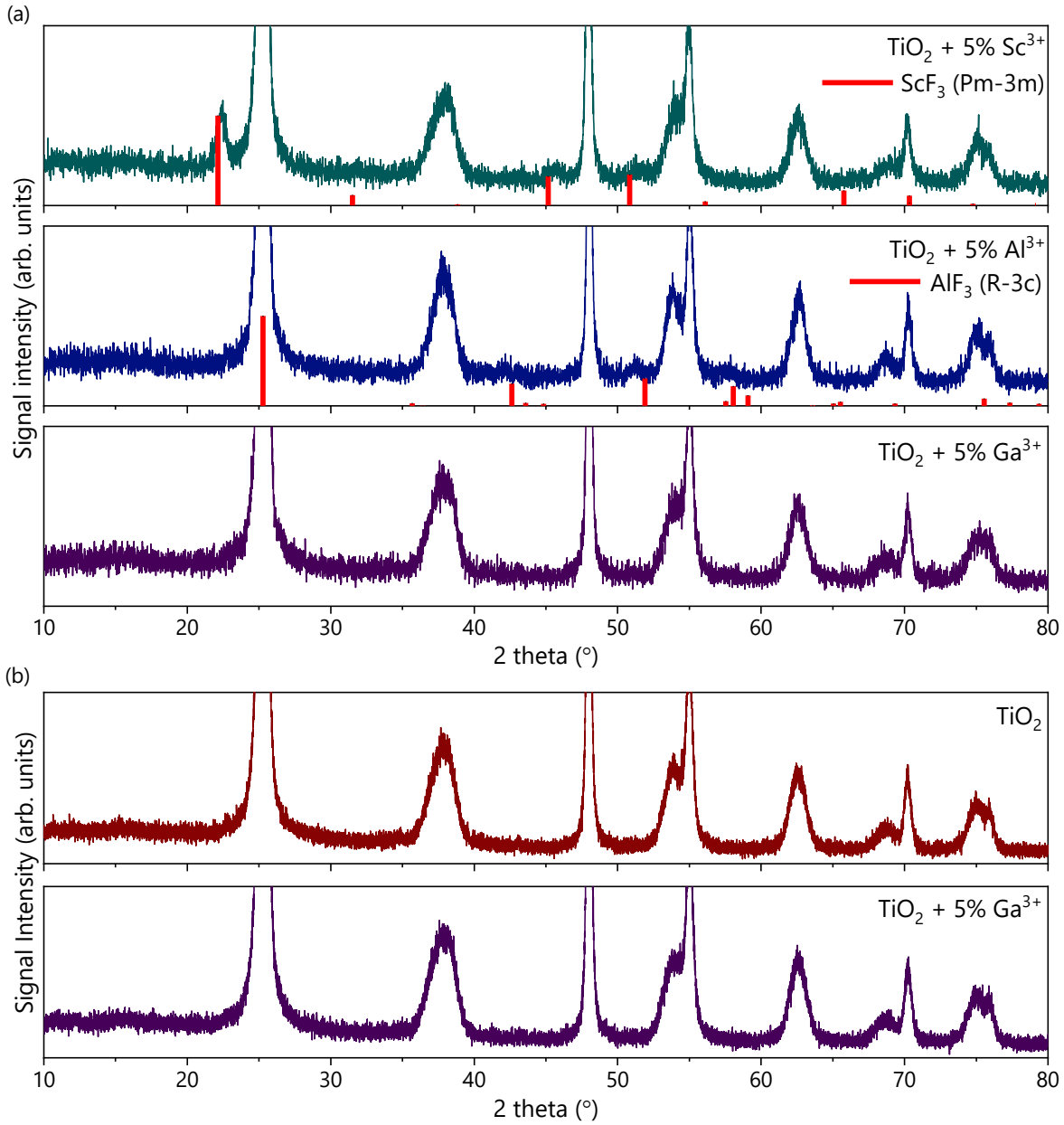

Figure S1. *Close-up of the XRD patterns considering different M^{3+} dopants with highlighted signals originating from the identified MF_3 phases: higher scan speed (a). Detailed comparison between XRD patterns of the non-modified TiO_2 sample and sample with 5% of Ga introduced to the synthesis: low scan speed (b).*

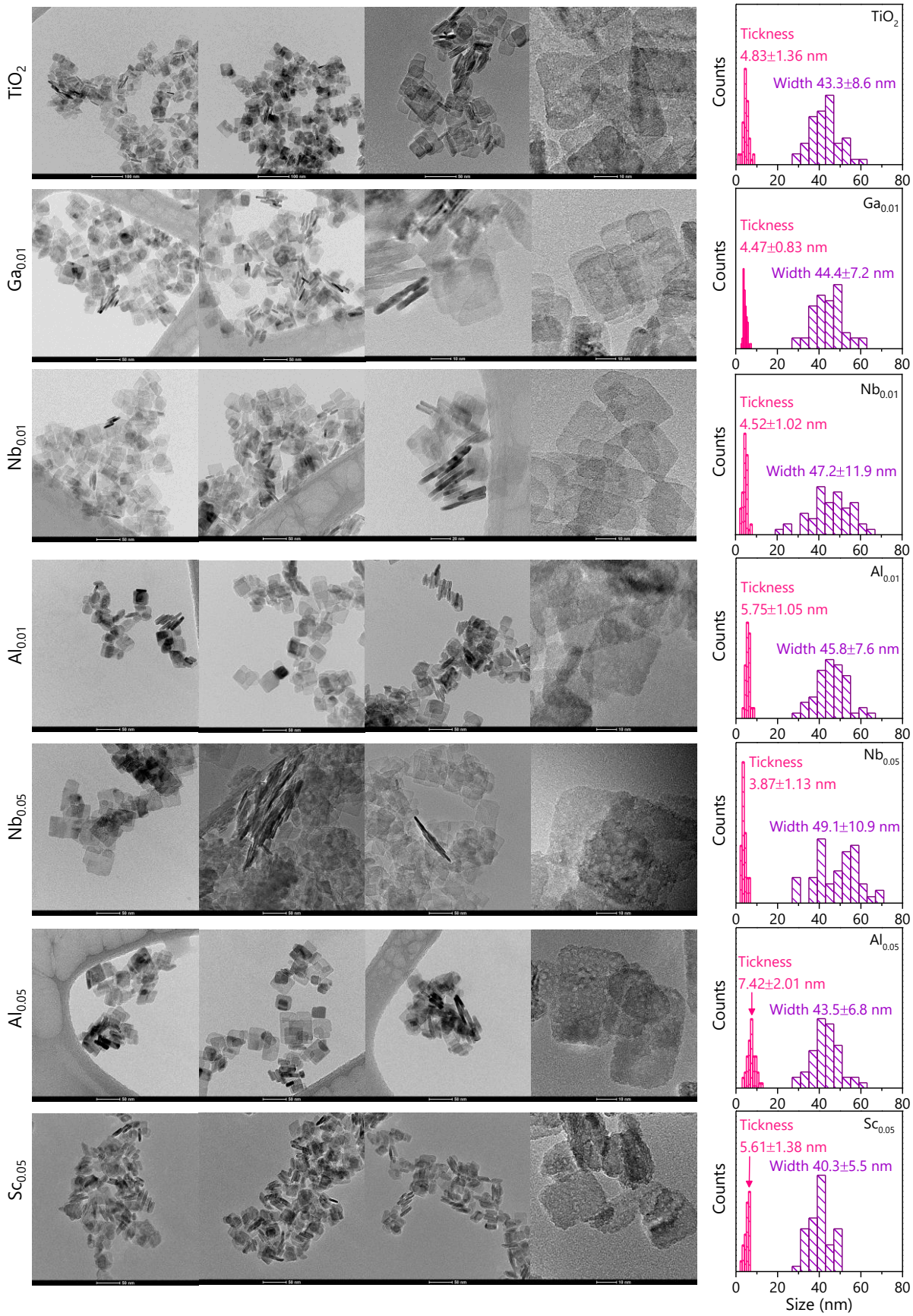

Figure S2. *Additional TEM images and shape analysis of the unmodified TiO_2 sample and selected doped materials.*

Table S1. *Numerical data on the refinement control, resulting structural parameters and BET surface areas of the prepared TiO_2 samples.*

Composition	R expected	R profile	R weighted	χ^2	Anatase *a* (Å)	Anatase *c* (Å)	Unit cell volume (Å^3)	$TiOF_2$ (wt. %)	BET ($m^2 \cdot g^{-1}$)
$Ga_{0.01}$	8.40	12.63	19.86	5.593	3.7887	9.5208	136.6627	0	132
TiO_2	8.68	11.95	18.51	4.546	3.7889	9.5178	136.6363	0	122
$Nb_{0.01}$	8.56	12.60	19.64	5.263	3.7894	9.5192	136.6916	0	129
$Nb_{0.02}$	8.51	13.04	19.47	5.233	3.7906	9.5290	136.9222	0	139
$Nb_{0.03}$	8.54	18.07	24.65	8.334	3.7921	9.5338	137.0935	3.6	139
$Nb_{0.05}$	8.50	14.65	20.63	5.887	3.7941	9.5619	137.6411	19.9	118

S6. Bandgap determination:

Graphical representation of the determined bandgaps of the bare and Nb/Ga doped single-phase photocatalysts is presented in **Figure S3a** using the Tauc's method.[20] In all cases, the formula for indirect semiconductors was used, based on the simulated band structures. Moreover, the absorbance spectra of all doped samples are shown for comparison **Figure S3b**.

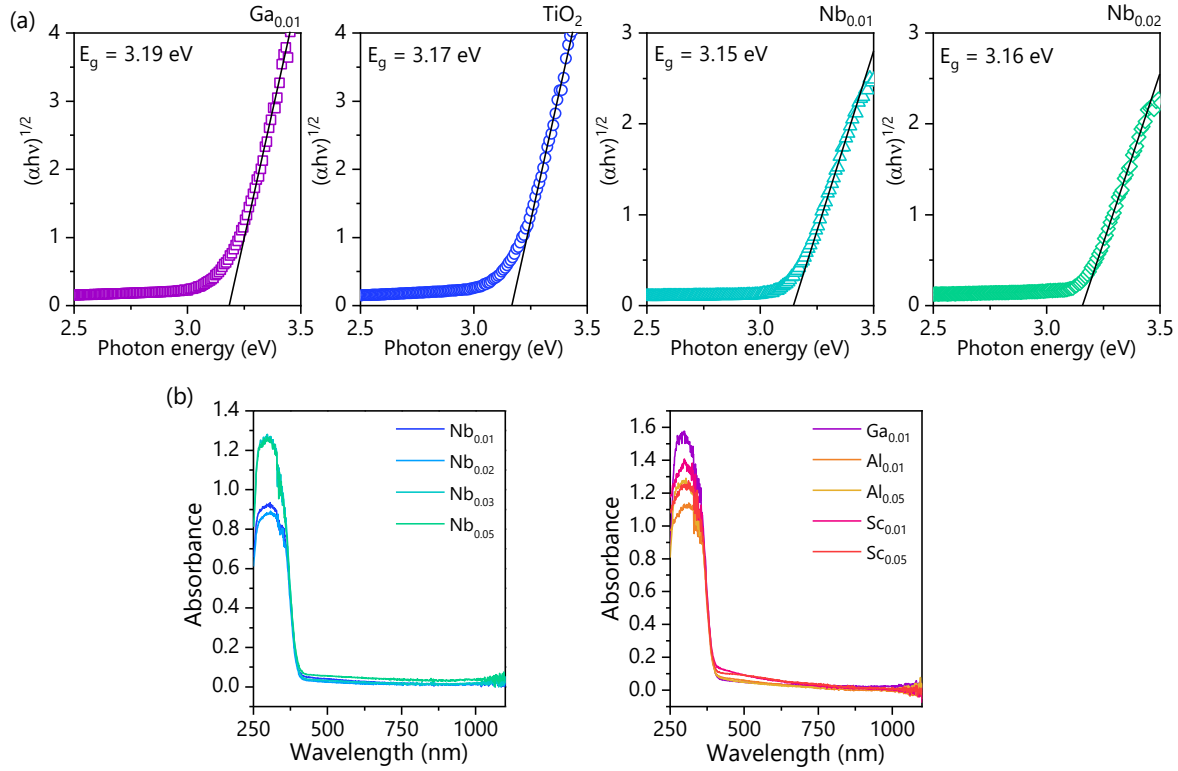

Figure S3*. Bandgap determination of the single-phase TiO_2/Nb/Ga materials, determined from the Tauc's method (a) and absorbance spectra of all doped samples (b).*

S7. Additional DFT results for bulk structure, clean {0 0 1} and defect position:

The bulk of anatase TiO_2 was modelled as in **Figure S4a**. The calculated charges of Ti and O atoms are +2.28 *e* and -1.14 *e*, respectively, which are consistent with the results in Ref. 21.[21]

For the surface, we used 3 × 3 periodic models of the surface, which were converged and compared to additional calculations with the 4 × 4 periodic model. A side view of the model is depicted in **Figure S4b**, which lists selected atomic charges. Farther from the top and bottom edges of the surface, the charges are the same as the ones calculated for the bulk, whereas at the edges they change slightly. The surface energy is 1.03 J/m^2, in consonance with Lazzeri *et al.*[12]

Substitution of Ti by Nb and Ga was then considered at different sites, as indicated in **Figure S4c**, and the formation energies at each site were compared. The formation energy of

a substitutional Nb atom at the central Ti layer (*i.e.*, farther from the top and bottom edges of the surface model) was found to be the same as in the bulk, and 0.60 eV less stable than at the outermost Ti layer. On either of the second-outermost Ti layers, it becomes marginally more stable than in bulk, with -0.04 eV difference. In general, the results imply that Nb atoms are thermodynamically more stable on the TiO_2 surface than in its bulk. On the other hand, Ga presents a different picture. The most stable position was found in the bulk. However, the differences are significantly lower. Therefore, Ga does not appear to particularly prefer sitting on the surface (there is not propensity to Ga segregation).

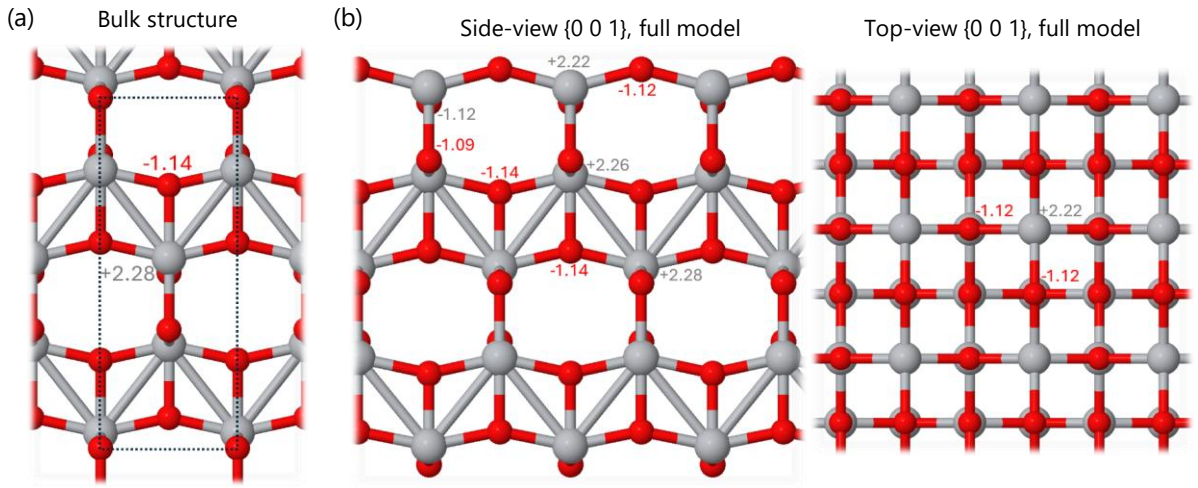

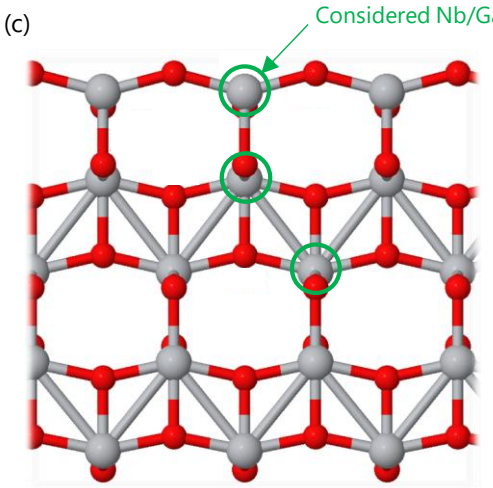

Energy relative to most-stable site		
Site	**Nb**	**Ga**
Surface	0.00 eV	0.14 eV
Sub-surface	0.56 eV	0.01 eV
Bulk-like	0.60 eV	0.00 eV

Figure S4. *Scheme of the models used in the DFT calculations: bulk structure (a) and {0 0 1} surface structure (b). Highlighted numbers show Bader charges in atomic units (1 e = 1.602 × 10^{-19}). Scheme of the positions considered for the Ti substitution by Nb and Ga, with calculated relative energy effects (c). Ti is grey, O is red.*

S8. Additional XPS results before and after CuO_x deposition:

Figure S5 show high-resolution XPS spectra of the Ti 2p, F 1s, Nb 3d and Ga 3d regions. All measured elements show a single chemical state: Ti^{4+}, Nb^{5+} and Ga^{3+} for metals and surface-adsorbed F^-.

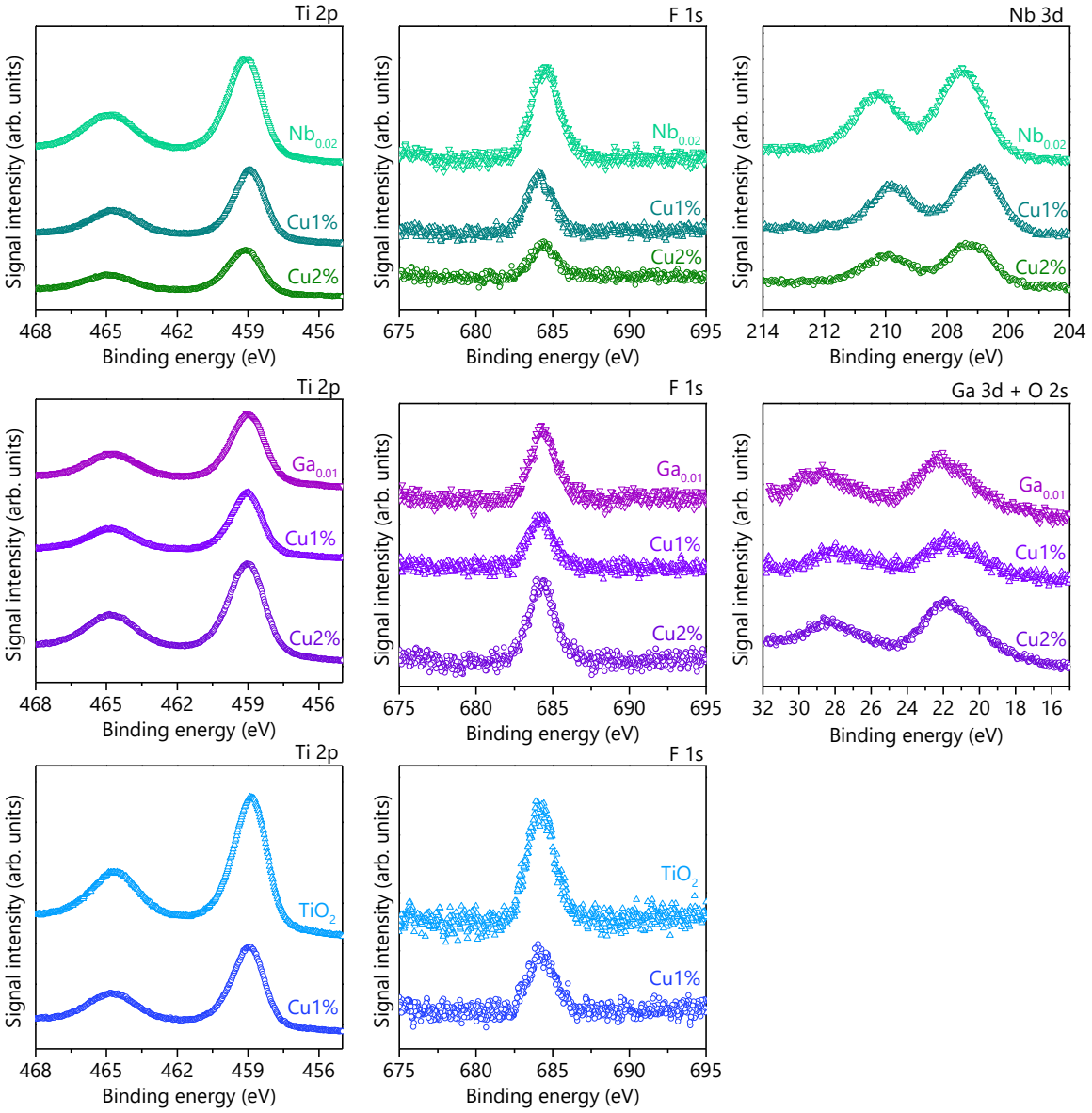

Figure S5. *High-resolution XPS spectra of the observed Ti 2p, F 1s, Nb 3d and Ga 3d states, considering both photocatalyst composition and Cu presence.*

S9. Additional DFT results for the Cu_1 modified surfaces:

Cu atoms adsorb at the center of a Ti_4O_4 ring, as shown in **Figure S6a**, with a charge of +0.64 *e*. Both geometry and charge do not change upon Nb doping (**Figure S6b**), but energy is considerably decreased, both with Nb atoms on the subsurface and on the surface Ti layers. Finally, in the case of the TiO_2:Ga {0 0 1}, the adsorption of a Cu atom leads to a rather distorted structure (**Figure S6c**) and is accompanied by a very negative adsorption energy, -2.78 eV, indicating system stabilization. If the model contains a substitutional Ga atom on the subsurface or deeper, the adsorption configuration, energy, and Cu charge tend towards the ones without Ga.

On the bare surface with Cu_1 adsorbed, an O_2 molecule adsorbs very exothermically and its O-O bond length is increased from 1.23 Å (gas phase value) to 1.45 Å. The charge on Cu becomes +1.06 *e* and this atom binds to four O atoms – two of the O_2 molecule and two of the outermost O layer of TiO_2, as shown in **Figure S6d**. The adsorbed O_2 molecule is very prone to dissociation, with an activation energy of merely 0.25 eV and a dissociation energy of -0.89 eV. The resulting geometry is highly symmetric, with the Cu atom is again found bonded to four O atoms, which are all equivalent by symmetry (**Figure S6e**). This configuration appears to be very stable, so that no extra O_2 or H_2 molecules can chemisorb and be activated by the surface, instead physisorbing weakly, with adsorption energies of -0.20 eV or -0.01 eV, respectively. It is not possible to chemisorb H_2 before the first O_2.

With an Nb atom on the outermost Ti layer, molecular O_2 adsorption on the Cu adatom is exothermic by -2.65 eV, and its dissociation is easier than in the absence of Nb, almost spontaneous, and releases more energy, -2.64 eV. The charge and geometry of the Cu atom along the process remain the same as on the surface without Nb (**Figure S6f**).

Molecular oxygen adsorption on a Cu atom with a Ga atom on the surface is very weak, with an adsorption energy of only -0.23 eV, and a geometry that hinders its further dissociation (**Figure S6g**). Similarly to Cu atom adsorption, as one considers Ga atoms placed deeper inside the TiO_2 surface, its presence becomes less relevant, and O_2 adsorption occurs in a manner more similar to that of the material without Ga.

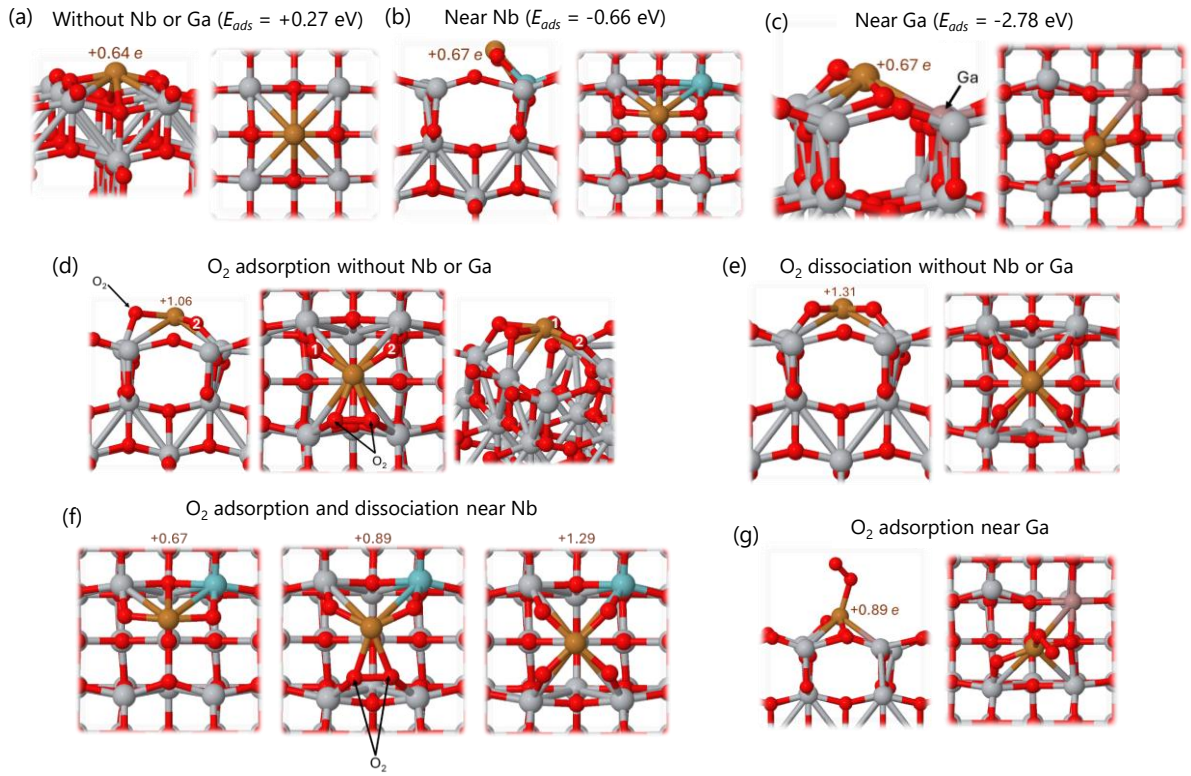

Figure S6. *Geometries of Cu_1 adsorptions on the bare and Nb/Ga substituted TiO_2 surfaces: Cu_1 on bare surface (a), Cu_1 in a proximity of a Nb_{Ti} defect (b) and near the Ga_{Ti} defect (c). Geometry of O_2 adsorption on the bare TiO_2 surface (d) and its dissociated configuration (e). Geometry of O_2 adsorption and dissociation near the Nb_{Ti} (f). Geometry of O_2 adsorption near the Ga_{Ti} (g). Ti atoms are grey, O are red, Nb are teal, Ga are pink-brown and Cu are orange-brown. Highlighted numbers are Bader charges on Cu_1.*

S10. Evolution of BET surface area due to doping and normalized ·OH generation:
Figure S7 show evolution of the BET surface area of TiO_2 samples due to the performed doping, with further comparison of the as-obtained and surface-normalized results of the ·OH generation.

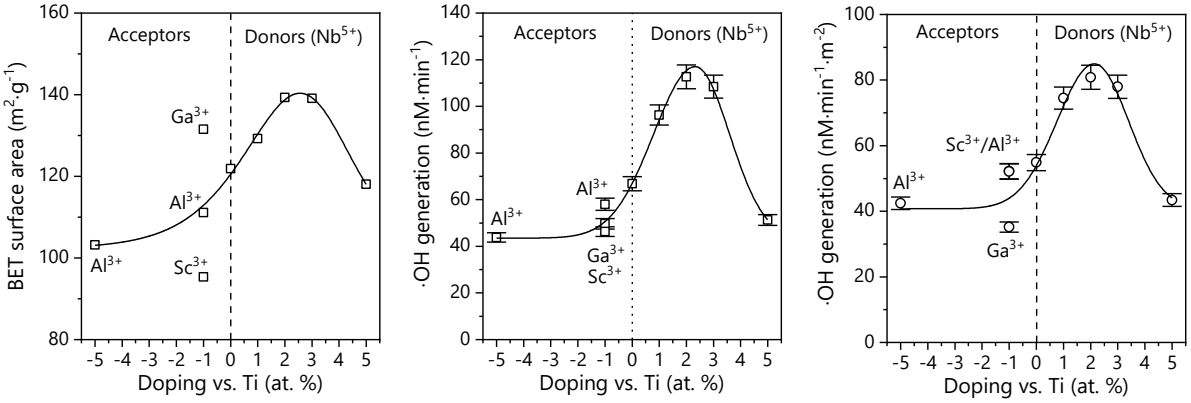

Figure S7. *BET surface areas and observed ·OH generation activities as a function of donor/acceptor doping of the prepared TiO_2 samples.*

S11. Additional DFT results for the interactions with H_2O:
The adsorption of a water molecule on the TiO_2 {0 0 1} + Cu surface model is exothermic by 2.21 eV. The resulting geometry clearly hints at molecular activation (**Figure S8**), as a hydrogen bond with length 1.66 Å appears to be established. The calculated dissociation energy barrier is lower than 0.01 eV and the dissociation into OH* + H* is exothermic by 1.09 eV.

On the contrary, near a substitutional Nb atom in its favored position, the Cu-H_2O interaction becomes much weaker, with an adsorption energy of only -0.28 eV. Here, every optimization of the atomic positions starting from a dissociated configuration spontaneously reverted to the configuration shown on the right side of **Figure S8**, with the H_2O molecule intact.

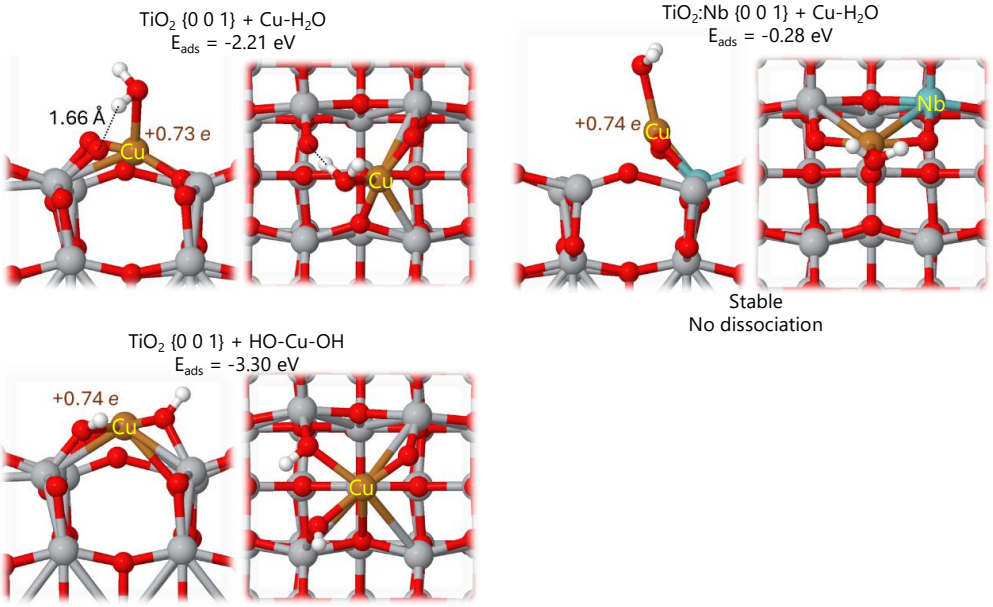

Figure S8. *Water adsorption geometries and energy effects on the Cu_1 atoms chemisorbed on the stochiometric {0 0 1} surface of TiO_2 and in the proximity of the surface Nb_{Ti} defect. Ti atoms are grey, O are red, Nb is teal and Cu are orange-brown.*

S12. Photoluminescence lifetimes:

Figure S9 show recorded emission spectra and emission decay curves for the obtained samples. Observed decays were fitted with the bi-exponential function (**Equation S1**):

$$y = y_0 + A_1 \cdot e^{\frac{-x}{t_1}} + A_1 \cdot e^{\frac{-x}{t_2}} \quad \text{(S1)}$$

where *A* and *t* are fitted parameters of both components. Based on the obtained parameters the average lifetime τ was calculated as:

$$\tau = \frac{\sum_{i=1}^{n}(A_i \cdot t_i^2)}{\sum_{i=1}^{n}(A_i \cdot t_i)} \quad \text{(S2)}$$

Where A_i is the amplitude (pre-exponential value) of each lifetime t_i.

Please note that for clarity, the total decay time **in Figure S9b** was presented only up to 10 ns and the fitted decay function were not presented. Total measurement time was 20 ns and the parameters of the fitted lines are presented in detail in **Table S2**.

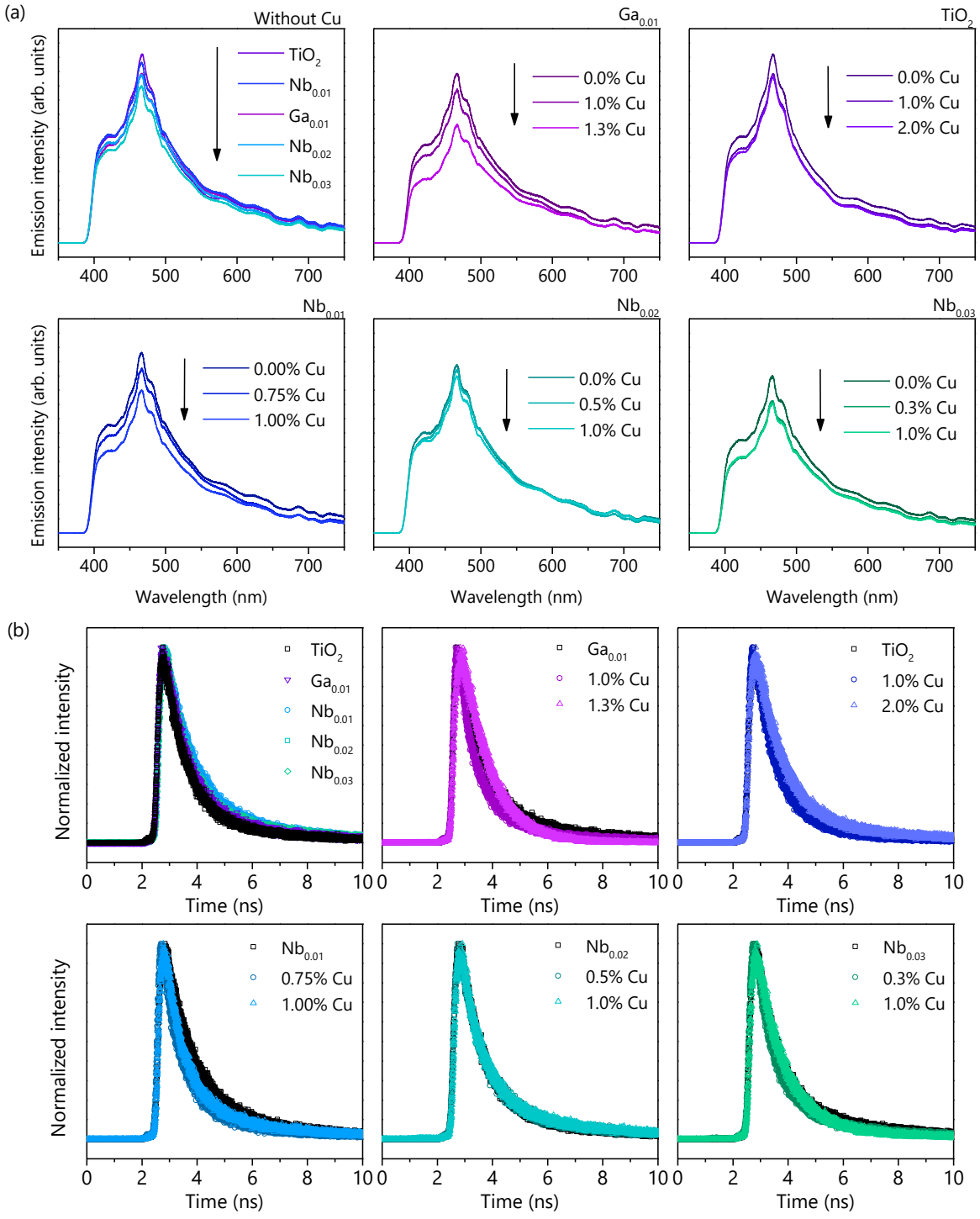

Figure S9. *Photoluminescence spectra (a) and decay curves (b) of the prepared samples. Excitation wavelength for spectra recording was 310 nm with 400 nm cut-off filter at the emission side. Excitation wavelength for the decay curves was 372 nm, with a band-pass filter between 425-475 nm.*

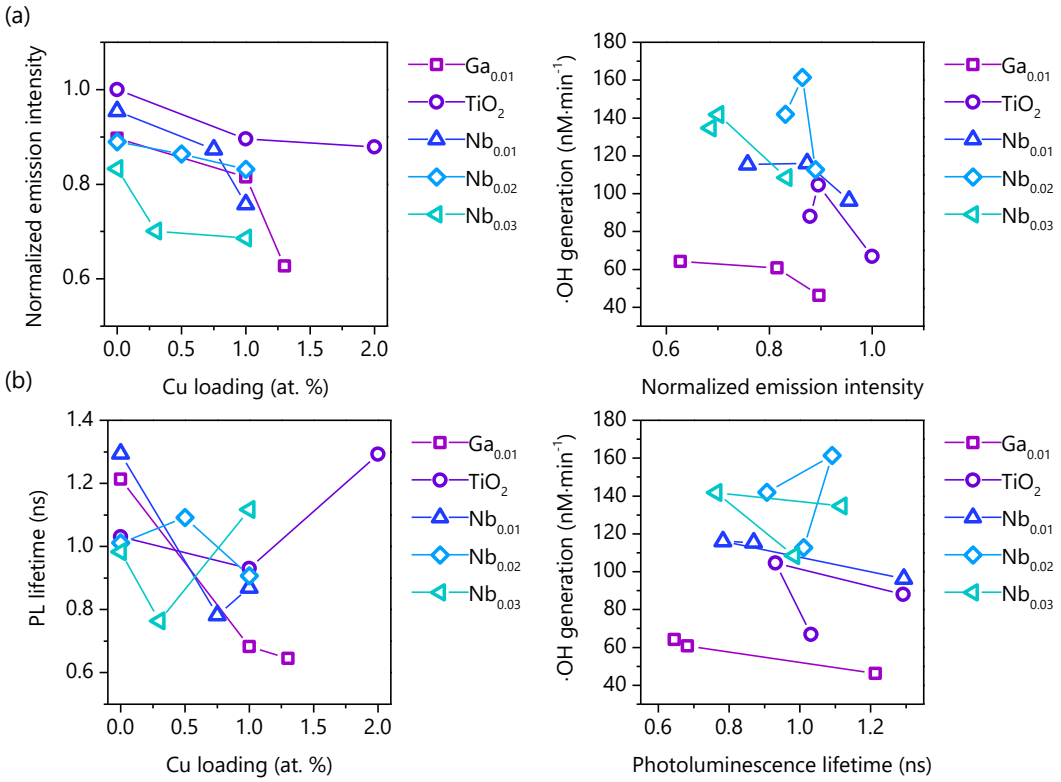

Figure S10. *Observed relations between the recorded emission maximum, normalized to the highest value (a), or the calculated emission lifetime (b), and Cu loading/ ability to generate ·OH for each TiO_2 hosts.*

Table S2. *Numerical data from the fitted photoluminescence decay curves.*

Sample	τ_1 (ns)	A_1	Contribution %	τ_2 (ns)	A_2	Contribution %	τ (ns)	R^2
$Ga_{0.01}$	0.97	15450	99	5.65	145	1	1.21	0.996
TiO_2	0.88	20480	99	4.70	158	1	1.03	0.996
$Nb_{0.01}$	1.05	13031	99	4.48	239	1	1.29	0.997
$Nb_{0.02}$	0.85	23284	99	3.76	302	1	1.01	0.997
$Nb_{0.03}$	0.82	26157	99	3.58	377	1	0.98	0.997
$Ga_{0.01}$	0.97	15450	99	5.65	145	1	1.21	0.996
$Ga_{0.01}$ 1.00% Cu	0.62	63093	99	2.30	617	1	0.68	0.997
$Ga_{0.01}$ 1.30% Cu	0.59	88746	99	3.01	431	1	0.65	0.996
TiO_2	0.88	20480	99	4.70	158	1	1.03	0.996
TiO_2 1.00% Cu	0.84	23939	99	3.91	158	1	0.93	0.997
TiO_2 2.00% Cu	1.04	13704	99	5.52	155	1	1.29	0.997
$Nb_{0.01}$	1.05	13031	99	4.48	239	1	1.29	0.997
$Nb_{0.01}$ 0.75% Cu	0.69	40623	99	2.83	434	1	0.78	0.996
$Nb_{0.01}$ 1.00% Cu	0.75	34811	99	3.40	367	1	0.87	0.996
$Nb_{0.02}$	0.85	23284	99	3.76	302	1	1.01	0.997
$Nb_{0.02}$ 0.50% Cu	0.89	19317	99	3.99	306	1	1.09	0.996
$Nb_{0.02}$ 1.00% Cu	0.75	32997	99	3.06	586	1	0.91	0.996
$Nb_{0.03}$	0.82	26157	99	3.58	377	1	0.98	0.997
$Nb_{0.02}$ 0.30% Cu	0.68	49320	99	2.71	551	1	0.76	0.997
$Nb_{0.02}$ 1.00% Cu	1.01	15778	99	4.90	96	1	1.12	0.997

S13. Coumarin removal from the ·OH generation experiments:

A comparison between removed coumarin and the observed rate of ·OH generation is presented in **Figure S11**, showing a clear correlation between both responses, with a minor effect of Cu absence.

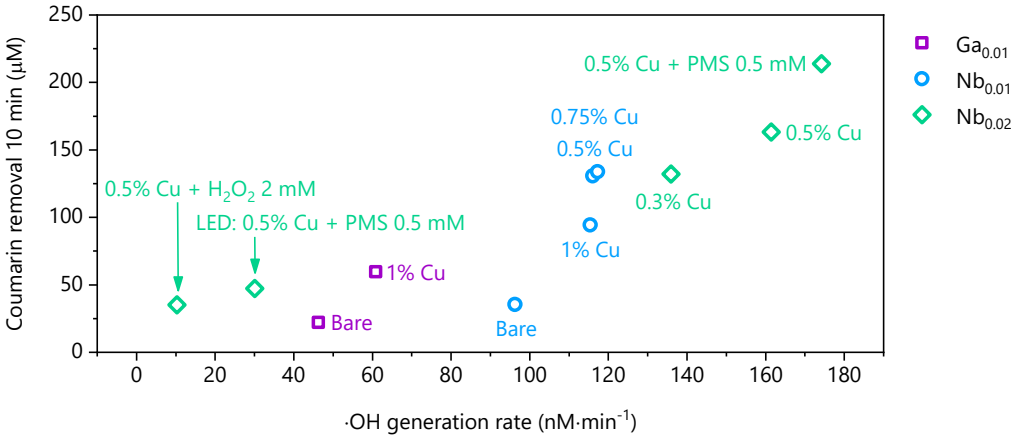

Figure S11. *Comparison between observed removal of the coumarin and ·OH generation rate for the selected systems.*

S14. Additional results for the $Al_{0.01}$ and $Sc_{0.01}$ samples:

Additional results for the $Al_{0.01}$ and $Sc_{0.01}$ samples including their XRD patterns before modification with Cu, corresponding unit cell volume compared to $Ga_{0.01}$, TiO_2 and $Nb_{0.01}$, as well as XPS spectra of the corresponding metals are shown in **Figure S12**.

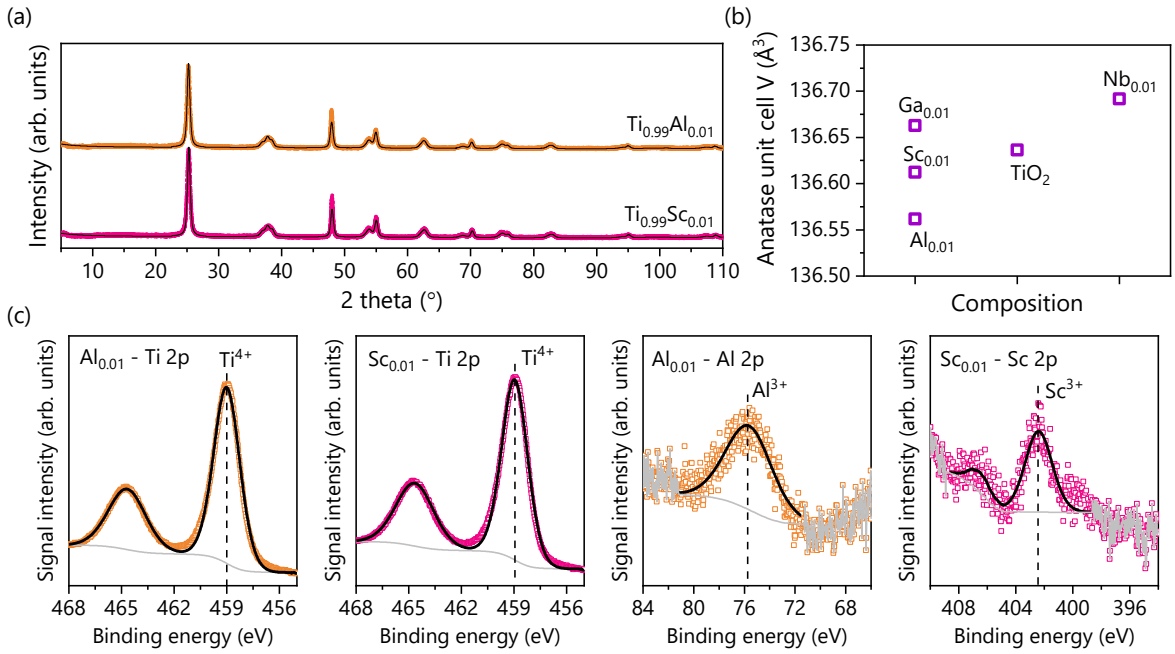

Figure S12. *Additional results for the $Sc_{0.01}$ and $Al_{0.01}$ samples, including XRD patterns (a), evolution of the unit cell volume (b) and XPS spectra of the Ti/Al/Sc (c).*

S15. Estimation of apparent quantum efficiency and relative photonic efficiency:

The apparent quantum efficiency (η) of the optimized photocatalyst was estimated in the analogical setup as other photocatalytic reactions, with the light source changed to a monochromatic 385 nm LED. The light from the diode was concentrated at the reactor centre

and its power flux was manipulated between I_{centre} = 2.9 mW·cm^{-2} and I_{centre} = 22.1 mW·cm^{-2} using dedicated software. For each case investigated, the flux distribution reaching the reactor border was mapped and fitted as the 2-dimensional Gauss function, to obtain the analytical expression (**Figure S13a** and **Figure S13b**)

$$I(x,y) = I_0 + A \cdot e^{-0.5\left(\frac{x-x_c}{\omega_x}\right)^2 - 0.5\left(\frac{y-y_c}{\omega_y}\right)^2}, \quad \text{(S3)}$$

where I_0, A, x_c, ω_x, y_c and ω_y are fitted parameters.

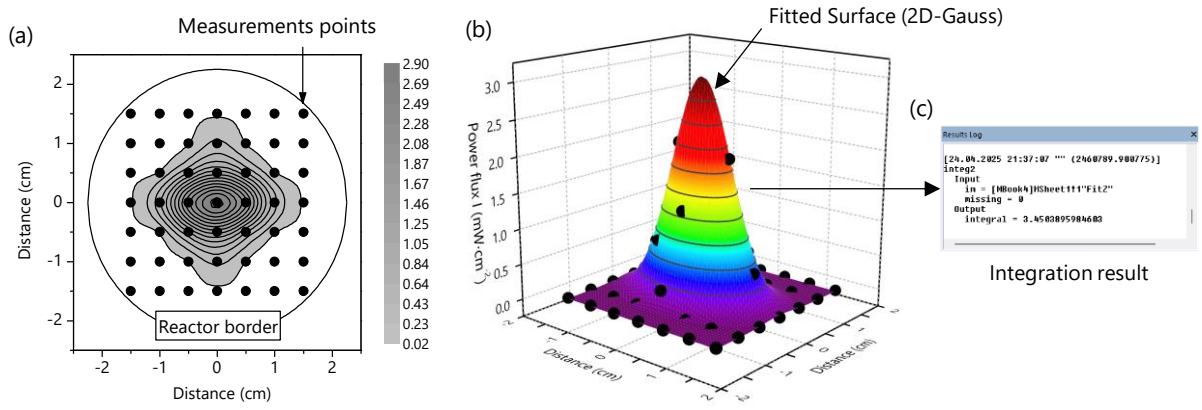

Figure S13. *Scheme of the procedure used to determine total power flux reaching reactor border: mapping of the flux intensity (a), fitting of the surface (b) and numeral integration of the fitted function (c). Example for the* I_{centre} *= 2.9 mW·cm^{-2}.*

The obtained function was integrated numerically over the reactor area (d = 4.5 cm) to estimate total power flux reaching the reaction medium I_{Total} (**Figure S13c**).

$$I_{Total} = \iint I(x,y)dxdy \quad \text{(S4)}$$

The value obtained, in mW, was then divided by 1000 and multiplied by 60, to obtain the final value in J·min^{-1}.

$$I_{Total}\left[\text{mW} = \frac{\text{mJ}}{\text{s}}\right] \cdot \frac{60}{1000} = I_{Total}\left[\frac{\text{J}}{\text{min}}\right] \quad \text{(S5)}$$

The choice of J·min^{-1} as a unit was entirely discretionary. The power flux was converted to photon flux I_{Photon} by considering the energy of each photon equal to λ = 385 nm.

$$E_{385\,nm} = \frac{h \cdot \nu}{\lambda} = 3.2208\ \frac{\text{eV}}{\text{n}} = 5.16013 \cdot 10^{-19}\ \frac{\text{J}}{\text{n}} \quad \text{(S6)}$$

where h is Planck constant, ν is frequency and λ is wavelength. Then, actual I_{Photon} values were obtained by dividing total power flux with $E_{385\,nm}$, giving value in photons per minute. The final used I_{Photon} value, in µmol per minute, was then obtained by dividing by Avogadro constant N_A·10^{-6}.

$$I_{Photon}\left[\frac{\text{n}}{\text{min}}\right] = \frac{I_{Total}\left[\frac{\text{J}}{\text{min}}\right]}{E_{385\,nm}\left[\frac{\text{J}}{\text{n}}\right]} \quad \text{(S7)}$$

$$I_{Photon}\left[\frac{\mu\text{mol}}{\text{min}}\right] = I_{Photon}\left[\frac{\text{n}}{\text{min}}\right] \cdot \frac{1}{N_A \cdot 10^{-6}} \quad \text{(S8)}$$

Table S3 show step-by-step calculations for a different I_{centre} values, up to the final I_{Photon}.

Table S3. *Numerical data connected with the determination of* I_{Photon} *for a different* I_{centre} *values of the 385 nm LED used during the determination of apparent quantum efficiency.*

I_{centre} (mW·cm^{-2})	I_{Total} (mW)	I_{Total} (J·min^{-1})	$E_{385\ nm}$ (J·n^{-1})	I_{Photon} (n·min^{-1})	$N_A \cdot 10^{-6}$	I_{Photon} (µmol·min^{-1})
2.9	3.45	0.207	$5.16013 \cdot 10^{-19}$	$4.01188 \cdot 10^{17}$	$6.022 \cdot 10^{17}$	**0.666**
6.3	7.50	0.445	$5.16013 \cdot 10^{-19}$	$8.71547 \cdot 10^{17}$	$6.022 \cdot 10^{17}$	**1.447**
13.3	15.82	0.950	$5.16013 \cdot 10^{-19}$	$1.83993 \cdot 10^{17}$	$6.022 \cdot 10^{17}$	**3.055**
22.1	26.29	1.578	$5.16013 \cdot 10^{-19}$	$3.05733 \cdot 10^{17}$	$6.022 \cdot 10^{17}$	**5.077**

To obtain η, calculated values of photon fluxes were multiplied by the reaction time (in minutes) and directly compared with the number of removed molecules of the parent compounds ΔN_P:

$$\eta = \frac{\Delta N_P}{I_{Photon} \cdot t} \cdot 100\% \quad \text{(S7)}$$

In each case, the ΔN_P was calculated *vs.* t = 0 min, that is at the start of the degradation process, after the adsorption. The final expression for the ΔN_P at given time includes calculating concentration difference in µM, multiplied by the reactor volume V_R.

$$\Delta N_P[\mu\text{mol}] = (C_0 - C_t)\ [\mu\text{M}] \cdot V_R \quad \text{(S8)}$$

The value obtained is directly comparable with the I_{Photon} values presented above. In the case of the initial tests of η vs I_{centre}, estimation was based on the single C_t value for coumarin, obtained after the 10 minutes of the process. Detailed data, together with the observed amount of generated 7-hydroxycoumarin, are presented in **Table S4**.

Table S4. *Numerical data connected with the η determination for coumarin with different* I_{centre} *values.*

I_{centre} (mW·cm^{-2})	C_{Flask} (µM)	C_0 (µM)	C_{10min} (µM)	V_R (dm^3)	ΔN_P (µmol)	t (min)	I_{Photon} (µmol·min^{-1})	η (%)	7-OHC conc. (nM)
2.9	472.42	451.04	436.83	0.04	0.568	10	0.666	**8.5**	256.6
6.3	472.42	454.09	430.35	0.04	0.950	10	1.447	**6.7**	416.2
13.3	472.42	448.52	432.45	0.04	0.643	10	3.055	**2.1**	439.1
22.1	472.42	450.78	434.15	0.04	0.665	10	5.077	**1.3**	597.4

Considering detailed degradation processes of coumarin, phenol, naphthalene, EE2 and methomyl, the set of different η values was calculated for each sample collected from t = 0 to t = 30 min. Then, the final value was presented as the mean of all observed values for different t, rounded to unity. Detailed data are presented in **Table S5**. All η values were calculated *vs.* t = 0 min. All experiments were performed with LED light for I_{centre} = 2.9 mW·cm^{-2} (I_{Photon} = 0.666 µmol·min^{-1}) and with 0.5 mM of PMS. The value obtained for t = 10 min during coumarin degradation was used to compare with the data presented in **Table S4**.

Table S5. *Numerical data connected with the η determination for different compounds during the degradation process with* I_{centre} *= 2.9 mW·cm*$^{-2}$.

Time (min)	Coumarin (μM)	η (%)	Phenol (μM)	η (%)	Naphthalene (μM)	η (%)	EE2 (μM)	η (%)	Methomyl (μM)	η (%)
-10	472.42		222.48		216.12		32.92		122.68	
-7	445.50		219.64		132.17		26.58		112.98	
-4	447.00		220.21		112.90		23.50		113.92	
0	447.93		221.54		94.66		24.93		119.80	
2	441.02	**20.8**	207.03	**43.6**	44.46	**150.7**	8.86	**48.3**	19.17	**302.1**
10	425.13	**13.7**	199.45	**13.3**	35.90	**35.3**	5.55	**11.6**	10.84	**65.4**
20	412.61	**10.6**	183.65	**11.4**	18.18	**23.0**	4.24	**6.2**	7.95	**33.6**
30	390.18	**11.6**	170.68	**10.2**	10.74	**16.8**	2.13	**4.6**	5.88	**22.8**
	Mean η	**14**	Mean η	**20**	Mean η	**56**	Mean η	**18**	Mean η	**>100**

Beside the η, additional calculations of the relative photonic efficiency (ξ) were performed to provide strictly material-oriented degradation efficiency, without additional PMS assistance. These studies involved testing degradation of all pollutants over the same $Nb_{0.02}$ + Cu 0.5% photocatalyst and relative comparison to the degradation rates using commercial P25 photocatalyst as standard. Studies were preformed under Xe lamp irradiation with 310 nm cutoff filter, analogical to the other presented results, beside detailed η estimation. However, during these experiments, photocatalyst concentration was increased to 2 g·dm^{-3}, which in case of our setup is optimal concentration for P25. Table S6 show detailed numerical results of these experiments and calculated ξ values for every possible interaction. For example, effect of pollutant type when using only P25:

$$\xi = \frac{k_{P25}}{k_{P25-phenol}} \cdot 100\% \quad \text{(S9)}$$

described as "P25 vs. P25-phenol". Alternatively, photocatalyst effect without considering pollutant structure:

$$\xi = \frac{k_{Nb0.02+Cu0.5\%}}{k_{P25}} \cdot 100\% \quad \text{(S10)}$$

and other analogical.

Table S6. *Numerical data connected with the determination of ξ.*

Pollutant	k (min^{-1})		ξ (%)			
	P25	$Nb_{0.02}$+$Cu_{0.5\%}$	P25 *vs.* P25-phenol	$Nb_{0.02}$+$Cu_{0.5\%}$ *vs.* $Nb_{0.02}$+$Cu_{0.5\%}$ -phenol	$Nb_{0.02}$+$Cu_{0.5\%}$ *vs.* P25-phenol	$Nb_{0.02}$+$Cu_{0.5\%}$ *vs.* P25
Phenol	0.06540	0.19534	100	100	299	299
Naphthalene	0.10727	0.46187	164	236	706	431
EE2	0.06122	0.11136	94	57	170	182
Methomyl	0.09995	0.68194	153	349	1043	683

S16. Exemplary DAD chromatograms:

Figure S14 shows DAD maps observed during photocatalytic degradation processes, either under 385 nm LED irradiation with 0.5 mM of PMS (η determination) or during the Xe lamp irradiation without PMS (ξ determination). In each case, formation of new by-products is observed (yellow arrows), which generally differ between the PMS-assisted and non-assisted processes. The pink line observed for the phenol at t = 0 min map is an artifact, originating from the baseline drift due to the slightly too short stabilization period. We note that this drift was stable and therefore, the determination of the absorption peaks was not affected.

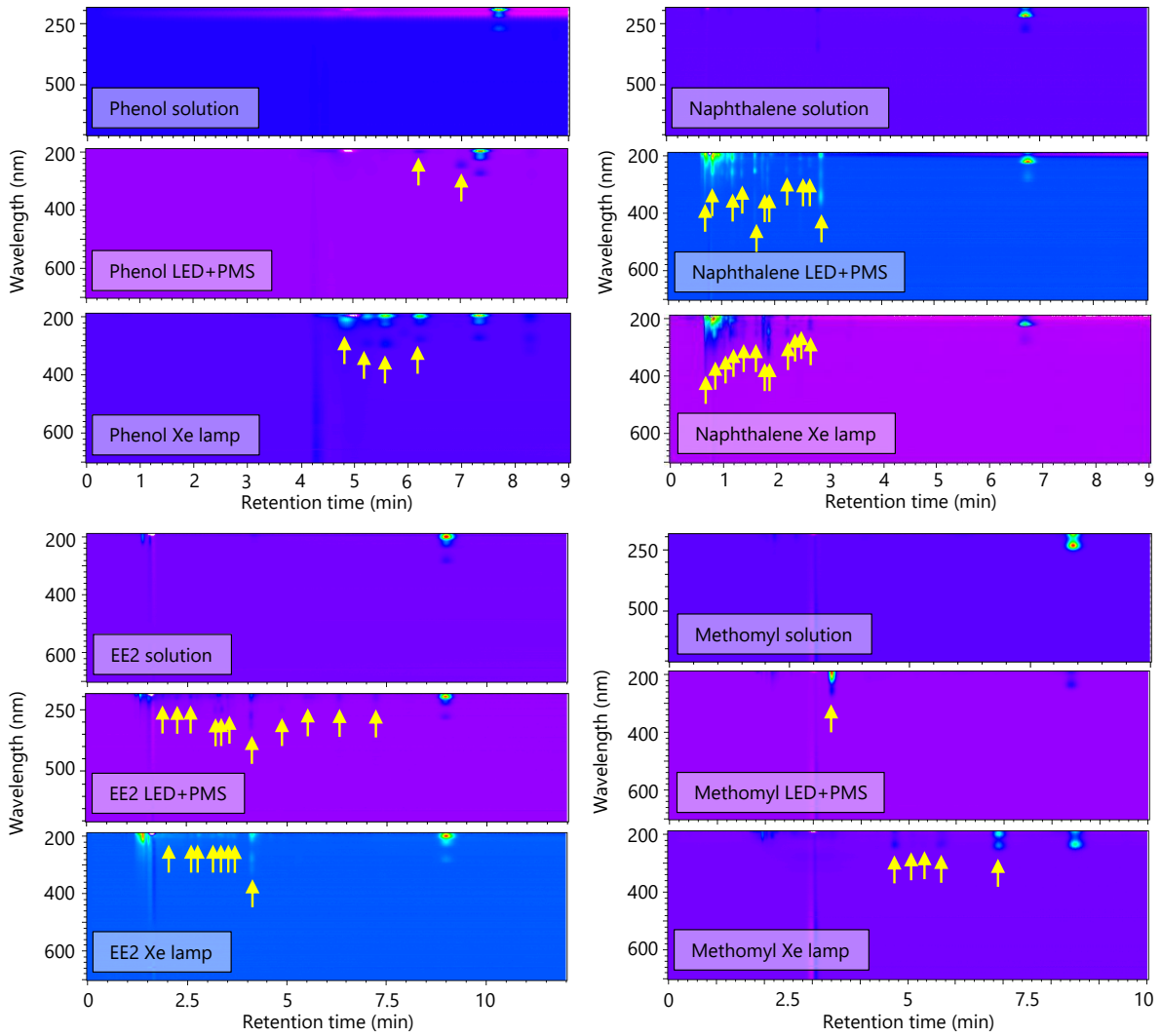

Figure S14. *DAD absorption maps obtained from the HPLC analysis of the photocatalytic degradation processes: comparison between the initial solution, process under 385 nm LED irradiation with 0.5 mM PMS and under the Xe lamp irradiation without PMS. New signals, appearing due to the degradation, are highlighted with arrows.*

Additional SI references:

1 S. Dudziak, M. Kowalkińska, J. Karczewski, M. Pisarek, K. Siuzdak, A. Kubiak, K. Siwińska-Ciesielczyk and A. Zielińska-Jurek, *Applied Surface Science*, 2021, **563**, 150360.

2 H. G. Yang, G. Liu, S. Z. Qiao, C. H. Sun, Y. G. Jin, S. C. Smith, J. Zou, H. M. Cheng and G. Q. Lu, *Journal of the American Chemical Society*, 2009, **131**, 4078–4083.

3 C. J. Howard, T. M. Sabine and F. Dickson, *Acta Crystallographica Section B Structural Science*, 1991, **47**, 462–468.
4 K. Vorres and J. Donohue, *Acta Cryst*, 1955, **8**, 25–26.
5 M. Klinger and A. Jäger, *J Appl Cryst*, 2015, **48**, 2012–2018.
6 M. Klinger, *J Appl Cryst*, 2017, **50**, 1226–1234.
7 G. Kresse and J. Furthmüller, *Physical Review B - Condensed Matter and Materials Physics*, 1996, **54**, 11169–11186.
8 J. P. Perdew, K. Burke and M. Ernzerhof, *Physical Review Letters*, 1996, **77**, 3865–3868.
9 J. D. Gouveia and J. Coutinho, *Electron. Struct.*, 2019, **1**, 015008.
10 I. Proença, J. D. Gouveia, M. R. Soares, L. Rino, F. M. Costa, T. Monteiro and J. Rodrigues, *physica status solidi (RRL) – Rapid Research Letters*, **n/a**, 2500102.
11 J. D. Gouveia and J. R. B. Gomes, *Materials Today Physics*, 2024, **46**, 101481.
12 M. Lazzeri, A. Vittadini and A. Selloni, *Physical Review B - Condensed Matter and Materials Physics*, 2001, **63**, 1554091–1554099.
13 P. E. Blöchl, *Physical Review B*, 1994, **50**, 17953–17979.
14 H. J. Monkhorst and J. D. Pack, *Physical Review B*, 1976, **13**, 5188–5192.
15 G. Henkelman and H. Jónsson, *The Journal of Chemical Physics*, 1999, **111**, 7010–7022.
16 J. Zhang and Y. Nosaka, *Applied Catalysis B: Environmental*, 2015, **166–167**, 32–36.
17 R. O. Olojo, R. H. Xia and J. J. Abramson, *Analytical Biochemistry*, 2005, **339**, 338–344.
18 P. Daniel, A. Bulou, M. Rousseau, J. Nouet, J. L. Fourquet, M. Leblanc and R. Burriel, *J. Phys.: Condens. Matter*, 1990, **2**, 5663.
19 L. Hu, J. Chen, L. Fan, Y. Ren, Y. Rong, Z. Pan, J. Deng, R. Yu and X. Xing, *J. Am. Chem. Soc.*, 2014, **136**, 13566–13569.
20 J. Tauc, R. Grigorovici and A. Vancu, *Physica Status Solidi (B) Basic Research*, 1966, **627**, 363–386.
21 D. Koch and S. Manzhos, *J. Phys. Chem. Lett.*, 2017, **8**, 1593–1598.